Experimental study on the formability of AA6016 sheets pre-strained by rolling

D. Vysochinskiy[1], T. Coudert[2], O.S. Hopperstad[1], O.-G Lademo[1, 2], A. Reyes[1,*]

[1] *Structural Impact Laboratory (SIMLab), Department of Structural Engineering, NTNU, Norwegian University of Science and Technology, NO-7491 Trondheim, Norway*

[2]*SINTEF Materials & Chemistry, NO-7465 Trondheim, Norway*

Abstract

The effects of prestrain by rolling on the formability of AA6016 sheets in the biaxial stretching region are studied in this paper. An experimental program including formability experiments has been carried out for as-received and prestrained sheets. Forming limit strains are determined by the digital image correlation technique and then mapped into stress space using an anisotropic plasticity model in order to assess the path-independence of forming limit stresses. Different diagrams for description of formability such as the traditional strain-based forming limit diagram (FLD), the forming limit stress diagram (FLSD) and various equivalent plastic strain based (EPS-based) diagrams are applied in order to study the effect of prestrain. It is shown that prestrain by rolling has the same effect on the forming limit strains as prestrain by plane strain tension. Furthermore, the forming limits of the virgin material nearly coincide with the forming limits of the prestrained material in the FLSD and EPS-based diagrams, serving as a conservative estimate for the prestrained material. Due to the roping phenomenon, the material displays significant anisotropy in forming limit strains. At the same time, the presence of roping does not affect the path-independence of the forming limits in the FLSD and EPS-based diagrams.

Keywords: formability; AA6016 sheet metal; pre-strain; forming limit diagram; local necking; roping

1. Introduction

Sheet metal formability is commonly described by means of the forming limit diagram (FLD) or forming limit curve (FLC), dividing safe and unsafe strain combinations. The traditional FLD first introduced by Keeler [1] (tension-tension domain) and Goodwin [2] (tension-compression domain) has the major and minor principal strains, ε_1 and ε_2, on its axes.

---

* Corresponding author: Aase Reyes (aase.reyes@ntnu.no), Tel.:+47 73 59 45 24, Fax: +47 73 59 47 01

One limitation of the traditional FLD is that proportional straining is assumed through the entire deformation process, i.e., the ratio between strain increments $\bar{\beta} = d\varepsilon_2/d\varepsilon_1$ is constant. The effects of non-proportional straining (i.e., $\bar{\beta}$ is not constant) could be studied for two-stage strain paths where formability tests are preceded by prestrain. A comprehensive experimental study on the effect of prestrain on strain-based FLCs for aluminium alloy sheets was published by Graf and Hosford [3,4].

For real stamping operations, straining is seldom proportional due to the complex geometry of the formed parts. As was shown by Leppin et al. [5], simply using a spherical punch makes the straining non-proportional and causes the FLCs obtained by Nakajima tests [6] to deviate from the ones obtained by Marciniak-Kuczynski tests [7], where a flat punch is used and strain paths are nearly linear. For industrial stamping operations with complex geometries, the deviation from a linear strain path is expected to be even greater. Thus, a path-independent formability description is desired.

Stoughton [8] mapped the experimental results of Graf and Hosford [3,4] into stress space using several constitutive models and showed that the different experimental FLCs degenerate into a single band in stress space. Based on this, he proposed to use the forming limit stress diagram (FLSD) and a stress-based FLC instead of the traditional FLD and strain-based FLC. The path-independence of forming limit stresses had been observed earlier by Arrieux et al. [9], and has been studied and discussed by different authors. Butuc et al. [10] mapped both experimentally and numerically predicted forming limit strains into stress space and found forming limit stresses to be path-independent. Wu et al. [11] mapped predicted FLCs into the stress space and performed reverse mapping of the predicted stress-based FLCs into the strain space. They found the predicted stress-based FLCs to be "almost path-independent" for moderate prestrains and path-dependent when the level of prestrain was close to the forming limit. Yoshida et al. [12] studied predicted strain-based and stress-based FLCs for combined loading consisting of two linear load paths with and without unloading between the path change. The predicted forming limit stresses were found to be path-independent for the case with unloading and path-dependent when no unloading took place. In the work by Yoshida and Kuwabara [13], the forming limit stresses were determined directly from the pressure and axial loading on a steel tube, which resulted in strain limits in the tension-tension, tension-compression and compression-tension region. The conclusion was that the forming limit stresses are path-independent when the hardening is not affected by the change of load path and path-dependent otherwise. Werber et al. [14] studied the effect of different pre-strains on the forming limit strains for AA6014 PX (pre-aged state), and later mapped these data into stress space [15]. They found that the forming limit stresses are not path-independent, but a systematic strain-path dependency was found. They also found that the choice of flow stress curve and yield criterion can have a great impact on the results in the mapping process.

However, the general agreement in the literature is that forming limit stresses are much less path-dependent than forming limit strains, although they can demonstrate path-dependence in some cases; such as for high levels of pre-strain [11], no unloading between two stages [12] and when hardening is affected by the strain-path change [13].

A disadvantage of the description of formability by means of stress-based FLCs is that due to saturation of the hardening curve $\bar{\sigma} = \bar{\sigma}(\bar{\varepsilon})$, where $\bar{\sigma}$ and $\bar{\varepsilon}$ are the equivalent stress and plastic strain, respectively, large differences in strains correspond to small differences in stresses [15]. To overcome this disadvantage the equivalent plastic strain based diagrams (EPS-based diagrams) have been proposed in the literature. Yoshida and Kuwabara [13] proposed to use a diagram with the equivalent plastic strain $\bar{\varepsilon}$ and stress ratio $\bar{\alpha} = \sigma_1 / \sigma_2$ on its axes, where σ_1 and σ_2 are the major and minor principal stresses, respectively. For the same purpose, Zeng et al. [16] proposed to plot the equivalent plastic strain $\bar{\varepsilon}$ vs. the ratio of principal strain increments $\bar{\beta} = d\varepsilon_2 / d\varepsilon_1$. The same type of diagram was simultaneously suggested by Leppin et al. [5]. Stoughton and Yoon [17] reviewed the diagrams proposed in [13] and [16] and introduced an alternative path-independent representation of forming limits denoted the polar equivalent plastic strain diagram (PEPSD). The coordinates (x, y) of the PEPSD are defined as $x = \bar{\varepsilon} \sin\theta$ and $y = \bar{\varepsilon} \cos\theta$ with $\theta = \arctan\bar{\beta}$. Since the strain increment ratio $\bar{\beta} \leq 1$, the angle $\theta \leq 45°$. In the FLD for an anisotropic material, the principal strains ε_1 and ε_2 may be replaced with the true strain in the rolling and transverse directions, ε_{RD} and ε_{TD}, as was done by Graf and Hosford [3,4]. For the PEPSD, the analogous operation would be replacing θ with $\bar{\theta} = \arctan(d\varepsilon_{TD} / d\varepsilon_{RD})$, where $\bar{\theta} \leq 90°$.

The present article presents an experimental study on the formability of pre-strained AA6016 sheets. We chose to use Marciniak-Kuczynski tests as these tests are influenced neither by friction nor the curvature of a punch. The tested material displays weak plastic anisotropy and suffers from roping in biaxial tension, which was also observed in previous studies [18,19]. The effects of these phenomena on the forming limit properties are studied experimentally. It is found that the presence of roping causes the anisotropy of forming limits to be significantly stronger than expected from the plastic anisotropy alone. The path independence of the PEPSD-FLC proposed by Stoughton and Yoon [17] and other EPS-based FLCs is evaluated.

2. Material & experimental details

Formability tests of virgin and rolled sheets of AA6016 temper T4 delivered by Hydro Aluminium Rolled Products GmbH, Research & Development in Bonn were carried out. This material exhibits good forming properties and is therefore typically used for the car body. The nominal thickness of the virgin sheets was 1.5 mm, while the average measured thickness was 1.496 mm. As the material

is usually applied in inner parts of the car body, there are normally no requirements in regards to surface quality. The sheets were produced by hot rolling, then solution heat treated and stored for six months for natural ageing. After heat treatment and natural ageing, the prestrain was applied by cold rolling. Thus, the as-received material is here referred to as virgin AA6016, while the prestrained material is referred to as rolled AA6016. The directional references RD (rolling direction) and TD (transverse direction) generally refer to the material symmetry axes due to the production process. Although the directions of hot rolling (material production) and cold rolling (prestrain) coincide for the studied case, RD and TD refer to the former.

The average measured thickness of the prestrained sheets was 1.364 mm which corresponds to a prestrain of $\varepsilon_3 = -0.092$, where ε_3 is the principal strain in the thickness direction. Note that prestrain by rolling can be regarded as plane strain deformation and $\varepsilon_1 = -\varepsilon_3$ due to the constant volume assumption.

In order to assess the formability of prestrained AA6016 sheets an experimental program was carried out, and included material characterization tests and Marciniak-Kuczynski-type formability tests of both virgin and prestrained AA6016 sheets. An overview of the experimental program is given in Table 1.

The uniaxial tension tests were carried out on dog-bone samples with 70 mm gauge length and 12.5 mm width taken out in seven directions (0°, 15°, 30°, 45°, 60°, 75°, and 90°) oriented to the rolling direction, both for the virgin and the prestrained material. The tests were performed in a Dartec testing machine, with a strain rate of approximately 10^{-3} s^{-1}. A virtual extensometer using digital image correlation (DIC) and a traditional mechanical extensometer were applied during testing. Repeat tests were performed for the virgin and rolled AA6016 material. The engineering and true stress-strain curves are shown in Figure 1. Only one of the repetitions is presented for each test direction as there was little scatter between the two repeat tests. As one can see from the plots, there is not much influence of the test direction on the stress-strain curves, but rolling increases the stress levels considerably.

Different strain and stress ratios are used to characterize the plastic anisotropy of the sheet material. The width-to-thickness strain ratios, also called Lankford coefficients after [20], are defined as

$$R_\alpha = \frac{\varepsilon_w}{\varepsilon_t} \tag{1}$$

where α refers to the sample axis orientation with regard to the rolling direction RD; ε_w is the true strain in the sample width direction and ε_t is the true strain in the thickness direction. The

experimental width-to-thickness strain ratios were found by means of the virtual extensometer which measured the length and width displacement throughout the tests. The stress ratios are defined as

$$r_\alpha = \frac{\sigma_\alpha^{YS}}{\sigma_0^{YS}}\bigg|_{W_p} \tag{2}$$

where σ_α^{YS} is the flow stress in a sample oriented in the tensile direction α and σ_0^{YS} is the flow stress in a sample oriented in the reference direction $\alpha = 0°$. The subscript denotes that the flow stresses are compared at the same level of specific plastic work W_p. The average value of the measured strain and stress ratios for the repeat tests are shown in Figure 2. The tested AA6016 sheets display weak plastic anisotropy mainly through the variation in R_α, while the directional variation of r_α is minor. It is further seen that the plastic anisotropy, as demonstrated by the stress and strain ratios, is not markedly influenced by the prestraining.

The equibiaxial strain ratio R_b is determined under equibiaxial tension, $\sigma_1 = \sigma_2$, and is defined as

$$R_b = \frac{\varepsilon_{TD}}{\varepsilon_{RD}} \tag{3}$$

where ε_{TD} is the true strain in the transverse direction and ε_{RD} is the true strain in the rolling direction. In order to determine an equibiaxial strain ratio, disk compression tests were carried out, as suggested by Barlat et al. [21]. An Instron 1332 universal tension-compression machine with total capacity of 250kN was used to perform the tests. 24 samples in total were tested: twelve samples of virgin and twelve of prestrained (rolled) AA6016. The samples were circular discs with an initial diameter equal to 10 mm. Each sample was compressed between two steel cylinders while a lubricant paste based on Molybdenum Disulfide (with a specified coefficient of friction of 0.09) was used in order to minimize the friction between the sample and the cylinders. The specimens were compressed to a desired compression force value, then unloaded and measured. The tests were force controlled; however, the strain rate in the tests was in the same range as the one used in the tensile tests. The twelve samples were divided into two sets with six samples in each set, where the first set was compressed up to a target compression force of 25kN and the second set was compressed up to a target compression force of 35kN. The thickness and in-plane dimensions were measured using a micrometer screw gauge, and strains in the rolling and transverse direction were calculated. Figure 3 shows the measurements of all the 24 samples.

The formability of the material was investigated by means of Marciniak-Kuczynski tests [7], that were performed in a BUP600 forming machine using a flat punch with a diameter of 100 mm. The punch velocity was 0.3 mm/s. The test set-up is illustrated in Figure 4. A friction sheet with a hole between the punch and the test specimen ensures a friction-free zone. Rectangular blanks with a

length of 205 mm were used as test specimens. Some of the samples together with underlying friction sheets after testing are displayed in Figure 5. The width of the samples was varied in order to attain different strain paths: 155 mm, 160 mm, 165 mm and 205 mm. Because of the material's anticipated anisotropic behaviour, both samples oriented parallel and normal to the rolling direction were used, denoted MK0 and MK90 respectively. In total, seven different strain paths were tested. Two and three repeat tests were performed for each strain path for the virgin and rolled AA6016, respectively. For equibiaxial tension, the number of repetitions was increased to four for both virgin and rolled AA6016. The following notation of the specimen labels has been used: "material"MK"width"-angle-"repetition no", e.g. vMK155-0-1, where "material" is either virgin (v) or rolled (r). MK stands for Marciniak-Kuczynski tests, "width" corresponds to the sample width, "angle" is either 0 or 90 depending on the sample orientation to the rolling direction, and "repetition no" distinguishes between the repeat tests.

The strains were measured by means of digital image correlation (DIC). DIC and 3D reconstruction methods are used to assess the displacement fields over the sample surface with 7D correlation software [22]. The stereo device is made of two Prosilica GC2450 cameras and was mounted on a special frame over the BUP machine, as illustrated in Figure 4 (a). Image pairs are recorded during the deformation process and an external device is used to generate synchronisation trigger pulses to the cameras at a frequency of 4 Hz. The image resolution is set to 2448×2050 grey level pixels and stored as 8 bit. The stereo camera device is calibrated before the forming test series. Calibration serves to establish the parameters of the stereo rig (focal length, lens distortion, relationship between the two cameras). The calibration procedure, used in this study, follows the method implemented in the 7D software (e.g. this procedure has been used and validated in the forming analysis of Pottier et al. [23]). A random black-and-white speckle pattern was applied to the sample surface using black and white matte painting sprays. The initial friction-free zone (circular with a 35 mm diameter) in the MK sample was used as analysis area. The resolution of the extensometric grid and the zone of interest around each point of this grid are both set to 15x15 pixels, corresponding to an element size of 0.7 mm on the initial mesh. The rate of the major strain was about 0.001-0.002 s^{-1} during the uniform deformation and went up to the 0.05 s^{-1} in the local necking areas prior to failure.

3. Constitutive model and determination of material parameters

A phenomenological elasto-plastic constitutive model was used, including an anisotropic yield criterion, the associated flow rule and isotropic hardening. Since the material is anisotropic, it is convenient to adopt the corotational stress formulation [24].

The rate-of-deformation tensor $\hat{\boldsymbol{D}}$ is additively decomposed into

$$\hat{\boldsymbol{D}} = \hat{\boldsymbol{D}}^e + \hat{\boldsymbol{D}}^p \tag{4}$$

where $\hat{\boldsymbol{D}}^e$ and $\hat{\boldsymbol{D}}^p$ are the elastic and plastic rate-of-deformation tensors, respectively. The hat denotes a corotational quantity. The hypoelastic relation is defined by

$$\dot{\hat{\boldsymbol{\sigma}}} = \frac{E\nu}{(1+\nu)(1-2\nu)}\left(\operatorname{tr}\hat{\boldsymbol{D}}^e\right)\boldsymbol{I} + \frac{E}{1+\nu}\hat{\boldsymbol{D}}^e \tag{5}$$

where $\dot{\hat{\boldsymbol{\sigma}}}$ is the stress rate tensor, E is Young's modulus and ν is Poisson's ratio. Since in sheet metal forming the elastic strains remain small, the nominal values of the elastic parameters were assumed: $E = 70000\,\text{MPa}$ and $\nu = 0.3$.

The plastic part of the rate-of-deformation tensor is determined by the associated flow rule as

$$\hat{\boldsymbol{D}}^p = \dot{\bar{\varepsilon}}\frac{\partial\bar{f}}{\partial\hat{\boldsymbol{\sigma}}} \tag{6}$$

where $\bar{f}$ is the yield function and $\dot{\bar{\varepsilon}}$ is the equivalent plastic strain rate. The loading-unloading conditions in Kuhn-Tucker form are expressed as

$$\bar{f} = \bar{\sigma}\left(\hat{\boldsymbol{\sigma}}\right) - \sigma^{YS}\left(\bar{\varepsilon}\right) \le 0, \quad \dot{\bar{\varepsilon}} \ge 0, \quad \dot{\bar{\varepsilon}}\bar{f} = 0 \tag{7}$$

where $\bar{\sigma}$ is the equivalent stress, defined by the anisotropic yield function, and σ^{YS} is the flow stress (or current yield stress).

The two-component Voce hardening rule was used to describe the evolution of the flow stress, viz.

$$\sigma^{YS}\left(\bar{\varepsilon}\right) = \sigma_0 + \sum_{i=1}^{2}Q_{Ri}\left(1 - \exp\left(-\frac{\theta_{Ri}}{Q_{Ri}}\bar{\varepsilon}\right)\right) \tag{8}$$

where σ_0 is the initial yield stress, θ_{Ri} and Q_{Ri} are hardening parameters. These parameters were identified from the uniaxial tension tests of the virgin AA6016 sheets. Only the samples oriented parallel to the rolling direction were used for this purpose. The hardening parameters were determined by fitting the curve to the experimental data minimizing the least square residuals. Data up until onset of diffuse necking were used. The determined hardening parameters are: $\sigma_0 = 139$ MPa,

$Q_{R1} = 44$ MPa, $Q_{R2} = 172$ MPa, $\theta_{R1} = 1071$ MPa and $\theta_{R2} = 1259$ MPa for the virgin material. The resulting fit is presented in Figure 6.

The constitutive model utilizes the high-exponent, anisotropic Yld2004-18p yield function introduced by Barlat et al. [25], which has 18 anisotropy coefficients in addition to the exponent a that defines the curvature of the yield surface. These parameters were determined by fitting the yield function to the experimental data, using the procedure described by Achani et al. [26] with the weight factor equal to unity. The input parameters for the identification were the width-to-thickness strain ratios R_α, the stress ratios r_α, the equibiaxial strain ratio R_b , as given in Equations (1)-(3), and the equibiaxial stress ratio r_b which is defined as

$$r_b = \left.\frac{\sigma_b^{YS}}{\sigma_0^{YS}}\right|_{W_p} \tag{9}$$

where $\sigma_b^{YS} = \sigma_{RD} = \sigma_{TD}$ is the equibiaxial flow stress and σ_0^{YS} is the flow stress in the reference direction under uniaxial tension.

For the applied Yld2004-18p yield function, the exponent a was set to 8 as aluminum has FCC crystal lattice and this is the common choice for FCC metals [27]. The equibiaxial stress ratio r_b was assumed equal to unity, i.e., the same as for an isotropic material, owing to lack of experimental data. However, Lademo et al. [28] performed texture-based polycrystal yield surface calculations for AA6016 T4, and $r_b = 1$ seems like a reasonable assumption. The strain ratios R_α and stress ratios r_α were determined from the uniaxial tension tests for seven directions in the plane of the sheet displayed in Figure 2, which includes the experimental strain and stress ratios for both the virgin and rolled material. The equibiaxial strain ratio R_b was determined from the disk compression tests, and the value of $R_b = 0.785$ was found by linear regression of the measurements of all the 24 samples, as illustrated in Figure 3.

The parameters of the calibrated yield criterion Yld2004-18p are listed in Table 2 while its shape is shown in Figure 7. The corresponding von Mises and Hershey (with $a = 8$) yield criteria are included in the figure for comparison. The fit for R_α and r_α to experimental data is demonstrated in Figure 2. The same yield function is used for both virgin and prestrained AA6016 following the assumption of isotropic hardening.

4. Formability tests

Marciniak-Kuczynski tests were carried out in order to characterize the formability of the virgin and the rolled material. After testing the specimens were inspected visually, and the fracture orientation was noted. These results are tabulated in Table 3 and 4. Here, the fracture orientation both to the

8

rolling direction and to the direction of the major principal strain is specified. Although the specimens fractured in a quite similar way, there were still marked differences between the different specimens, as to where the fracture occurred and to the fracture path (some were quite straight, while others were curved). Some fractures seemed smoother than others, and a few of the specimens had two distinct fractures, where it seemed like the fractures had started developing around the same time. One of the most interesting effects was that for three of the specimens with width 165 mm, the fracture path was oriented parallel to the major strain, which was an unexpected outcome. Furthermore, one could clearly see some sort of irregularities on the surface of the specimens.

The rough surface appears like small ridges, all oriented in the same direction, see Figure 8. According to Engler et al. [29], this is a phenomenon that is common for aluminum alloys like AA6016, and a tendency of groups of metal grains to deform together and form rope-like structures or ridges on the sheet surface which is called roping or ridging. Graf and Hosford also experienced roping in their experiments [3,4]. In all the tests that experienced roping, the ridges were aligned in the rolling direction, and these ridges are probably the reason for the unexpected direction of the fracture lines in the three specimens with width 165 mm. The surface roughening has not been considered a problem, as the investigated material is used in inner parts of the car body where surface quality generally is of no concern. However, roping causes inhomogeneous deformation and stimulates the formation of multiple local necks, which in turn makes it difficult to use the guidelines of the ISO 12004-2 [30] to determine necking [19].

During testing, the speckle pattern on the surface of the samples was recorded by two cameras, and the displacements and strains subsequently determined by DIC analysis. The final (immediately after fracture) strain maps for some of the tests are shown in Figure 9, where we can compare the strain maps of the virgin and rolled material. The strain maps for the repeat tests were quite similar, although not identical, so one repetition for each specimen width is displayed in the figure. Note that the strain legends are not the same for the different plots. It seems that the localization is to some extent clearer for the virgin material. Especially for the specimens with widths 155 mm and 160 mm, the localization of deformation and the development of a local neck into a somewhat straight fracture line seem quite clear. However, when looking at the strain map of specimen vMK165-0-1 it seems that the variation in the strain field is not that prominent. There is a clear localization however, and the picture indicates that the fracture orientation has changed from the other tests. On the last picture of the virgin specimens (vMK205-1) we can see hints of the roping and formation of multiple necks. For the rolled material, there is a relatively clear indication of local necking and a developing fracture line for the specimens with width 155 mm and 160 mm. However, the strain distribution seems less homogeneous throughout the test area. When it comes to specimen rMK165-0-2 one can see the localization; however, how the fracture will develop seems more random. Then for the test rMK205-1, the strains

have developed similarly to the corresponding virgin specimen, with one clear maximum localization line, and several other grooves which are probably caused by the roping phenomenon.

In order to study how the strains and fractures are developing for the specimens with more unclear localisation patterns, the pictures of the specimens are presented together with the strain maps in Figure 10. Note that for specimen rM165-0-1 and rMK165-0-2, the fracture line has been emphasized in black as the original pictures were somewhat faint. As one can see, it is common for the rolled material that the specimens of 165 mm width do not have a clear localization line or orientation. It seems that the fracture orientation could be almost random. This is not the case for the specimen of the virgin material having the same width, here it seems quite clear from the strain maps in which direction the fracture line will develop. Note that for specimen rMK165-90-2, the forming limits are taken from a localization point different from the fracture line, i.e., there were multiple necks (as one can see from the strain map) and the forming limits are taken from the point where the largest equivalent strain is found. The strain values in the two most prominent necks are quite close, and the fracture developed in the other prominent neck.

5. Forming limit diagrams

Six different types of forming limit diagrams have been constructed for the experiments performed in this study: (1) the "traditional" FLD for the anisotropic material, (2) the FLSD, (3) the equivalent strain vs. stress ratio [12], (4) the equivalent strain vs. strain ratio [5,16], (5) the original PEPSD [17], and (6) the PEPSD for anisotropic materials. Each of these diagrams displays an FLC which serves as a forming limit criterion, and the objective is to evaluate the properties of these FLCs.

The starting point for this evaluation of formability is the experimentally detected strain-based FLC of virgin and prestrained AA6016. The experimentally detected forming limit strains are mapped into stress space, using the anisotropic elastic-plastic model presented in Section 3 and the parameters given there. The stress-based FLCs for the virgin and rolled AA6016 are then compared in search of a path-independent formability criterion.

When detecting forming limit strains experimentally, it is important to do so in a user-independent and repeatable manner. As Liebertz et al. [31] demonstrated, different laboratories detect different forming limit strains for the same material unless common guidelines are followed. The widely accepted method for experimental detection of the forming limit strains is described in the international standard ISO12004-2:2008 [30]. However, the tested AA6016 experienced roping and multiple local necking, as illustrated in Figure 8 and 9, while the standard method requires single local neck failure. The standard [30] explicitly specifies to discard samples with multiple local necks. As these experiments were carried out for research purposes, and the objective was to study the formability of AA6016, another, more general approach to detect forming limits has been

developed [18,32], namely the thickness-control method [19]. In this method, local thinning is calculated throughout the test, and the onset of localized necking is said to occur when the degree of thinning surpasses a certain limit. A local thickness is measured over a small circular area with radius r^{point}, while a "uniform" thickness is evaluated over a larger circular area with radius r^{area}. When localization starts, the degree of thinning, the ratio between the two thicknesses, k, will start to deviate from unity. When this ratio exceeds the allowed degree of thinning, k_{limit}, local necking has occurred. A detailed description of the method can be found in [19].

In this study, the thickness-control method was used to find the strains at necking and fracture, with the following input parameters: $r^{point} = 1\,\text{mm}$, $r^{area} = 8\,\text{mm}$ and $k_{limit} = 0.98$, which have been used in a previous study [19]. The point of initiation of local necking, found from the method, is marked in the strain maps in Figure 9 and 10. Here, the two evaluation radii are also indicated. As mentioned earlier, the DIC analysis area is chosen as the friction-free zone on the plates, as the friction between the steel plate and the test specimen can influence the strains outside this zone. However, as one can tell from Figure 9 and 10, the localization is sometimes initiated at the border or close to the border of the friction-free zone, which means that the area created by r^{area} sometimes goes beyond the DIC analysis area. In these cases, the average of the thickness within the DIC analysis area is used, and the data from the friction zone is not included in the average. For most cases where the initiation of necking starts well within the friction-free area this is probably acceptable. However, it is difficult to know the reason for initiation of necking for the cases where necking initiates on the border of the friction-free area. Here, of course, friction could be a factor in the localization process, although the friction-free area expands somewhat during testing, while the DIC analysis area is taken as the initial friction-free area. Furthermore, for some of the tests on the rolled material, localization was initiated outside the friction-free area. In these cases, the DIC data from the area outside the friction-free zone has been used to determine the forming limits, but it is then more difficult to know the origin of the localization, and how much friction has influenced the results.

The necking and fracture strains found from the thickness-control method for all tests are tabulated in Table 3 and 4, where it is also registered if necking was initiated inside or outside of the friction-free area. It is also distinguished between the specimens where necking was localized practically on the border and which ones were inside the border, but r^{area} went outside the friction-free zone. The experimental forming limit strains are presented in Figure 11, where each point corresponds to one single test. Figure 11 (a) shows the FLD for the virgin material, Figure 11 (b) shows the FLD for the rolled material, while Figure 11 (c) compares the two FLDs. The cross in Figure 11 (b) and (c) indicates the pre-strain applied to the specimens, and this pre-strain is included in the points for the rolled material. In Figure 11 (a) and (b) it is distinguished between where the neck was localized and if r^{area} reached outside the friction-free zone (called "close to border of friction-free area"). It does

11

not seem to matter much on the forming limits whether the localization started within or outside the friction-free zone. The only point that appears to deviate from the trend of the tests is obtained with specimen rMK160-0-1, where the initiation of necking and the following fracture are localized outside of the friction-free zone and the initiation of necking starts much earlier (for smaller strains) than for the two other repetitions. For this particular specimen, friction might have influenced the localization.

In Figure 11 (c) the forming limits for the virgin and rolled material are plotted together so that one can see the effect of prestrain. The forming limit strains are translated somewhat upward (almost the amount of the prestrain) and inward for the points in the lower area of the diagram. The effect is not so prominent for the points in the upper area of the diagram. The observed effect resembles what was earlier observed by Graf and Hosford [3,4] and Werber et al. [15] for prestrain in plane strain tension. The prestrain by rolling can be seen as prestrain in plane strain tension with superimposed hydrostatic stress. Thus, it appears that the effect of prestraining under plane strain conditions on the forming limits is similar regardless of whether the prestrain was applied by tension or by rolling. It is further evident that the formability is considerably lower in TD than in RD. The reason for this is not the plastic anisotropy of the sheet material but the roping phenomenon. The result of roping is the evolution of grooves along RD with straining, which is detrimental for the formability, particularly when the major stress is directed along TD.

The experimentally detected limit strains need to be mapped into the stress space by utilizing the constitutive model in order to construct the stress-based FLCs. The forming limit stresses were found using a stand-alone material driver, where the stresses are calculated numerically, based on a specified strain path, plane stress conditions and the calibrated constitutive model. The strain paths were assumed to be linear for the virgin material and bilinear for the rolled (prestrained) material, as illustrated in Figure 12. In total, seven strain paths were used both for virgin and rolled AA6016, each strain path representing an average of the repeat tests. Furthermore, the strain path for a point in the necked zone was taken from the DIC calculations, for one representative test, and is included in Figure 12. The equivalent plastic strain $\bar{\varepsilon}$ is calculated during this mapping procedure, while the stress ratio $\bar{\alpha}$ and strain increment ratio $\bar{\beta}$ are given from the strain paths, hence the EPS-based FLCs were constructed simultaneously with the stress-based FLCs.

Figure 13 (a) and (b) present the stress paths calculated based on the specified strain paths for the virgin and rolled AA6016, respectively, using the calibrated constitutive model. Figure 13 (c) presents a comparison of the forming limit stresses for the virgin and rolled AA6016, and one can observe that the forming limit stresses indeed appear to be path-independent. In order to study the effect of the constitutive model, the forming limit stresses of the virgin and prestrained material were also calculated using the isotropic von Mises and Hershey yield criteria (Hershey with $a = 8$), and the

results can be seen in Figure 14. Here, the points are plotted in Figure 14 (a), while the forming limit stress curve is plotted in Figure 14 (b) for easier comparison. It is apparent that for the materials tested here, the results by using von Mises and Yld2004-18p yield criteria are quite similar, while the forming limit stresses from Hershey yield criterion gives lower stresses compared to the results from the two other criteria.

Another factor that could influence the results is the hardening extrapolation [15]. We have used the tensile test to calibrate the hardening law, while the strains of the MK tests are higher than the range achieved in the tensile tests. Werber et al. [15] investigated the effect of the extrapolation by fitting the tensile data to two different hardening laws. The mapping of limit strains to limit stresses was influenced by the different hardening law to a certain extent. When Weber et al. [15] instead used the the flow stress curve from a bulge test, where the strains were within the same range as the strains in the FLD, the choice of hardening law did not influence the results much. In our case, we have used the tensile test to fit the hardening law, with a range of strains somewhat lower than the forming limit strains. However, the same material was studied extensively by Lademo et al. [28]. They simulated a shear test, which undergoes large plastic strains, with different minimum strain hardening rates in the extrapolation range beyond diffuse necking. They found that the flow stress data, with a strain hardening rate in the same range as the strain hardening rate that we have in the current study, gave good results. We have therefore reason to believe that the fitted hardening data from the tensile tests also gives reasonable results for the forming limit stress diagram. Regardless, the path independence will not be affected by the strain hardening data.

As mentioned earlier, the stress-based FLCs have a relatively low resolution in the failure region, so that large differences in strains correspond to small differences in stresses, and it is difficult to use the forming limit stress diagram to assess the path-independence of the forming limit stresses. Thus, also the various EPS-based diagrams from the literature were evaluated [5,13,16,17]. When the forming limit stress is calculated, the corresponding equivalent plastic strain is also determined, thus enabling direct evaluation of the path-independence of the various EPS-based diagrams, see Figure 15. All these diagrams operate with the ratios of principal stresses or strains. Therefore, the samples with axes parallel (MK0) and normal (MK90) to the rolling direction need to be treated separately in these plots. As said before, it is possible to produce a continuous PEPSD plot by replacing the principal strains $(\varepsilon_1, \varepsilon_2)$ with $(\varepsilon_{RD}, \varepsilon_{TD})$ and θ with $\overline{\theta} = \arctan(d\varepsilon_{TD} / d\varepsilon_{RD})$. This expands the range of angles from $\theta \leq 45°$ to $\overline{\theta} \leq 90°$. The "expanded" PEPSD is presented in Figure 15 (d).

The forming limits of the EPS-based diagrams retain the path-independence observed for the forming limit stresses. Due to a better resolution of the EPS-based diagrams, it is possible to observe that the forming limits are not completely path-independent. This is especially noticeable for the samples with their axis normal to the rolling direction (MK90). However, for engineering purposes, the forming

limits of the EPS-based diagrams can be considered path-independent. It is also clear that forming limit stresses of the virgin material could be a conservative estimate of the formability of the prestrained material. Based on Figure 15, the expanded PEPSD [15] appears to be the best choice, since it is readily modified to display the formability of anisotropic materials and is similar to the traditional FLD.

6. Concluding remarks

Marciniak-Kuczynski formability tests [7] of virgin and prestrained sheets of aluminium alloy AA6016 were performed and different forming limit diagrams were compared with respect to path independence. The samples experienced roping and multiple local necks, so the forming limit strains were detected by the means of the thickness-control method [18,19,32]. The experimentally detected forming limit strains proved to be affected by prestrain as expected. The effect of prestrain by rolling on formability is similar to the effect of prestrain by plane strain tension reported in the literature.

Mapping of the experimentally detected forming limit strains into stress space confirmed path independence of the forming limit stresses. However, the low resolution of the FLSD in the failure region is an issue. The EPS-based diagrams do not have the same resolution problems, and therefore four different types of EPS-based diagrams were tested: the equivalent strain vs. stress ratio diagram [12], the equivalent strain vs. strain ratio diagram, the original and expanded PEPSD [17]. As explained in [17] there is a one-to-one mapping between points in the EPS-based diagrams and the FLSD, and thus EPS-based FLCs can be regarded as stress-based forming limits. It was observed that all the stress-based FLDs retained approximate path independence of the forming limits. The better resolution of the EPS-based diagrams disclosed that the forming limits of the virgin material appear to be a conservative estimate of the formability of the prestrained material. Thus, some effect of the strain path on the stress-based forming limits is observed, but the EPS-based diagrams can be considered path independent for engineering purposes.

For the tested AA6016, the experimentally detected anisotropy of the forming limit strains was significantly greater than expected; most likely because of roping in the sheets. At the same time, the presence of roping did not affect the path independence of the stress-based and EPS-based FLCs. This is in agreement with the results of Stoughton and Yoon [17] who observed path independence of the forming limit stresses based on the experiments by Graf and Hosford [3,4], where roping was also present in the tested material. However, the effect of roping on the forming limits in the present study is much more severe than what was observed by Graf and Hosford [3,4].

Among the different types of EPS-based diagrams, the PEPSD [17] appears to be most convenient, since it is designed to resemble the traditional FLD and can be easily modified to accommodate plastically anisotropic sheets, like the tested AA6016 sheet material.

Acknowledgements

Compliance with Ethical Standards

References

1. Keeler SP (1968) Circular Grid System - A Valuable Aid for Evaluationg Sheet-metal Formability. Sheet Metal Industries:633-641

2. Goodwin G (1968) Application of Strain Analysis to Sheet Metal Forming Problems in the Press Shop. SAE Technical Paper. doi: 10.4271/680093

3. Graf A, Hosford W (1993) Effect of Changing Strain Paths on Forming Limit Diagrams of Al 2008-T4. Metallurgical Transactions A 24:2503-2512

4. Graf A, Hosford W (1994) Influence of strain-path changes on forming limit diagrams of Al 6111 T4. International Journal of Mechanical Sciences 36 (10):897-8910

5. Leppin C, Li J, Daniel D (2008) Application of a method to correct the effect of non-proportional strain path on Nakajima test based forming limit curves. Numisheet 2008 - 7th International Conference and Workshop on Numerical Simulation of 3D Sheet Metal Forming Processes, Interlaken, Switzerland,

6. Nakajima K, Kikima T, Hasuka K (1968) Study on the formability of Steel Sheets. Yawata Technical Report 264:141-154

7. Marciniak Z, Kuczynski K (1967) Limit strains in the process of stretch-forming sheet metal. International Journal of Mechanical Sciences 9:600-620

8. Stoughton TB (2000) General forming limit criterion for sheet metal forming. International Journal of Mechanical Sciences 42 (1):1-17

9. Arrieux R, Bédrin C, Boivin M, Le Maître F (1985) Determination of the Strain Path Influence of the Forming Limit Diagrams, from the Limit Stress Curve. CIRP Annals - Manufacturing Technology 34 (1):205-208. doi: 10.1016/S0007-8506(07)61757-0

10. Butuc MC, Gracio JJ, Barata Da Rocha A (2006) An experimental and theoretical analysis on the application of stress-based forming limit criterion. International Journal of Mechanical Sciences 48 (4):414-429. doi: 10.1016/j.ijmecsci.2005.11.007

11. Wu PD, Graf A, MacEwen SR, Lloyd DJ, Jain M, Neale KW (2005) On forming limit stress diagram analysis. International Journal of Solids and Structures 42 (8):2225-2241

12. Yoshida K, Kuwabara T, Kuroda M (2007) Path-dependence of the forming limit stresses in a sheet metal. International Journal of Plasticity 23 (3):361-384

13. Yoshida K, Kuwabara T (2007) Effect of strain hardening behavior on forming limit stresses of steel tube subjected to nonproportional loading paths. International Journal of Plasticity 23 (7):1260-1284

14. Werber A, Liewald M, Nester W, Grünbaum M, Wiegand K, Simon J, Timm J, Bassi C, Hotz W (2012) Influence of different pre-stretching modes on the Forming Limit Diagram of AA6014. Key Engineering Materials, vol 504-506. doi: 10.4028/www.scientific.net/KEM.504-506.71

15. Werber A, Liewald M, Nester W, Grünbaum M, Wiegand K, Simon J, Timm J, Hotz W (2013) Assessment of forming limit stress curves as failure criterion for non-proportional forming processes. Production Engineering 7 (2-3):213-221

16. Zeng D, Chappuis L, Cedric Xia Z, Zhu X (2008) A path independent forming limit criterion for sheet metal forming simulations. World Congress, Detroit, MI, United states, April 14-17. doi: 10.4271/2008-01-1445

17. Stoughton TB, Yoon JW (2012) Path independent forming limits in strain and stress spaces. International Journal of Solids and Structures 49:3616-3625. doi: 10.1016/j.ijsolstr.2012.08.004

18. Vysochinskiy D (2014) Formability of aluminium alloy subjected to prestrain by rolling. PhD Thesis, Norwegian University of Science and Technology, Trondheim

19. Vysochinskiy D, Coudert T, Hopperstad OS, Lademo O-G, Reyes A (2016) Experimental detection of forming limit strains on samples with multiple local necks. Journal of Materials Processing Technology 227:216-226. doi: 10.1016/j.jmatprotec.2015.08.019

20. Lankford WS, S. Bauscher, J. (1950) New criteria for predicting the press performance of deep drawing sheets. Transactions of the American Society for Metals 42:1197-1232

21. Barlat F, Brem JC, Yoon JW, Chung K, Dick RE, Lege DJ, Pourboghrat F, Choi SH, Chu E (2003) Plane stress yield function for aluminum alloy sheets-part 1: theory. International Journal of Plasticity 19 (9):1297-1319

22. Vacher P, Dumoulin S, Morestin F, Mguil-Touchal S (1999) Bidimensional strain measurement using digital images. Proceedings of the Institution of Mechanical Engineers, Part C: Journal of Mechanical Engineering Science 213 (8):811-817

23. Pottier T, Vacher P, Toussaint F, Louche H, Coudert T (2012) Out-of-plane Testing Procedure for Inverse Identification Purpose: Application in Sheet Metal Plasticity. Experimental Mechanics 52 (7):951-963. doi: 10.1007/s11340-011-9555-3

24. Belytchko T, Liu WK, Moran B (2000) Nonlinear Finite Elements for Continua and Structures. Wiley, Chichester

25. Barlat F, Aretz H, Yoon JW, Karabin ME, Brem JC, Dick RE (2005) Linear transfomation-based anisotropic yield functions. International Journal of Plasticity 21 (5):1009-11039

26. Achani D, Hopperstad OS, Lademo OG (2009) Behaviour of extruded aluminium alloys under proportional and non-proportional strain paths. Journal of Materials Processing Technology 209 (10):4750-4764. doi: 10.1016/j.jmatprotec.2008.12.002

27. Hosford WF (1979) On yield loci of anisotropic cubic metals. 7th North American Metalworking Research Conference, Dearborn, MI, USA,

28. Lademo OG, Engler O, Keller S, Berstad T, Pedersen KO, Hopperstad OS (2009) Identification and validation of constitutive model and fracture criterion for AlMgSi alloy with application to sheet forming. Materials and Design 30 (8):3005-3019. doi: 10.1016/j.matdes.2008.12.020

29. Engler O, Schäfer C, Brinkman HJ (2012) Crystal-plasticity simulation of the correlation of microtexture and roping in AA 6xxx Al–Mg–Si sheet alloys for automotive applications. Acta Materialia 60 (13–14):5217-5232. doi: 10.1016/j.actamat.2012.06.039

30. International Standard ISO 12004-2 Metallic materials - Sheet and strip - Determination of forming-limit curves Part 2: Determination of forming-limit curves in the laboratory (2008) ISO 2008.

31. Liebertz H, Duwel A, Illig R, Hotz W, Keller S, Koehler A, Kröff A, Merklein M, Rauer J, Staubwasser L, Steinbeck G, Vegter H (2004) Guideline for the Determination of Forming Limit Curves. In: Proceedings of International Deep Drawing Research Group (IDDRG) Conference, Sindelfingen, Germany. 216-224

32. Vysochinskiy D, Coudert T, Hopperstad OS, Lademo O-G, Reyes A (2014) Experimental detection of the onset of local necking in an aluminium sheet. Materials Science Forum 794-796:590-595. doi: 10.4028/www.scientific.net/MSF.794-796.590

Tables

Table 1   Experimental program.

		AA6016: Virgin & pre-strained by rolling (9.2%)
Material tests	Uniaxial tension	• 7 directions: 0°, 15°, 30°, 45°, 60°, 75°, 90° • At least two repeat tests
	Disk compression	• 2 target compression loads: 25kN and 35kN • 6 repeat tests
Formability tests	Marciniak-Kuczynksi	• Length: 205 mm • Width: 155 mm, 160 mm, 165 mm, 205 mm • At least two repeat tests

Table 2: Parameters of the Yld2004-18p yield function for AA6016. The stress components are arranged according to Voigt notation: $\boldsymbol{\sigma} = [\sigma_{11}, \sigma_{22}, \sigma_{33}, \sigma_{23}, \sigma_{13}, \sigma_{12}]^{\mathrm{T}}$, where x_1 is along RD, x_2 along TD and x_3 in the thickness direction of the sheet material.

c'_{12}	c'_{13}	c'_{21}	c'_{23}	c'_{31}	c'_{32}	c'_{44}	c'_{55}	c'_{66}	a
1.0621	0.8589	0.6194	-0.1916	0.7447	1.0446	1.000	1.000	0.4515	8

c''_{12}	c''_{13}	c''_{21}	c''_{23}	c''_{31}	c''_{32}	c''_{44}	c''_{55}	c''_{66}
0.8041	1.2012	0.8310	0.8920	-0.0589	-0.8909	1.000	1.000	1.1884

Table 3: Crack orientation, necking and fracture strains for the MK samples of virgin AA6016.

Sample	Crack orientation		Necking strains		Fracture strains		Necking within friction-free area
	to RD	to ε_1	ε_1	ε_2	ε_1	ε_2	
vMK155-0-1	$\perp$	$\perp$	0.250	0.036	0.322	0.042	Yes
vMK155-0-2	$\perp$	$\perp$	0.268	0.041	0.369	0.043	Yes
vMK155-90-1	$\parallel$	$\perp$	0.143	0.020	0.284	0.024	Yes
vMK155-90-2	$\parallel$	$\perp$	0.152	0.023	0.298	0.024	Yes
vMK160-0-1	$\perp$	$\perp$	0.278	0.089	0.418	0.132	Yes
vMK160-0-2	$\perp$	$\perp$	0.286	0.094	0.398	0.132	Yes
vMK160-90-1	$\parallel$	$\perp$	0.142	0.041	0.313	0.061	Yes
vMK160-90-2	$\parallel$	$\perp$	0.138	0.039	0.287	0.054	Yes
vMK165-0-1	$\parallel$	$\parallel$	0.252	0.148	0.280	0.222	Yes, r^{area} outside
vMK165-0-2	$\parallel$	$\parallel$	0.277	0.166	0.324	0.257	Yes
vMK165-90-1	$\parallel$	$\perp$	0.177	0.091	0.297	0.120	On the border
vMK165-90-2	$\parallel$	$\perp$	0.149	0.074	0.247	0.103	On the border
vMK205-1	$\parallel$	-	0.193	0.173	0.283	0.219	On the border
vMK205-2	$\parallel$	-	0.174	0.155	0.296	0.217	Yes, r^{area} outside
vMK205-3	$\parallel$	-	0.158	0.140	0.307	0.219	Yes
vMK205-4	$\parallel$	-	0.190	0.169	0.311	0.239	Yes

Table 4: Crack orientation, necking and fracture strains for the MK samples of prestrained AA6016.

Sample	Crack orientation to RD	to ε_1	Necking strains ε_1	ε_2	Fracture strains ε_1	ε_2	Necking within friction-free area
rMK155-0-1	$\perp$	$\perp$	0.176	0.024	0.290	0.030	Yes, r^{area} outside
rMK155-0-2	$\perp$	$\perp$	0.173	0.018	0.273	0.026	Yes
rMK155-0-3	$\perp$	$\perp$	0.189	0.018	0.286	0.020	Yes
rMK155-90-1	$\parallel$	$\perp$	0.086	0.005	0.202	0.007	Yes, r^{area} outside
rMK155-90-2	$\parallel$	$\perp$	0.080	0.003	0.196	0.013	Yes, r^{area} outside
rMK155-90-3	$\parallel$	$\perp$	0.058	0.000	0.234	0.007	Yes
rMK160-0-1	$\perp$	$\perp$	0.137	0.040	0.316	0.091	No
rMK160-0-2	$\perp$	$\perp$	0.204	0.047	0.328	0.064	Yes, r^{area} outside
rMK160-0-3	$\perp$	$\perp$	0.200	0.046	0.318	0.053	Yes
rMK160-90-1	$\parallel$	$\perp$	0.070	0.009	0.225	0.025	Yes
rMK160-90-2	$\parallel$	$\perp$	0.090	0.015	0.220	0.030	On the border
rMK160-90-3	$\parallel$	$\perp$	0.078	0.013	0.190	0.026	Yes, r^{area} outside
rMK165-0-1	$\perp$	$\perp$	0.175	0.077	0.336	0.159	On the border
rMK165-0-2	$\parallel$	$\parallel$	0.194	0.094	0.289	0.175	Yes
rMK165-0-3	$\perp$	$\perp$	0.223	0.108	0.340	0.144	No
rMK165-90-1	$\parallel$	$\perp$	0.109	0.017	0.241	0.032	No
rMK165-90-2	$\parallel$	$\perp$	0.133	0.050	0.212	0.075	Yes, r^{area} outside
rMK165-90-3	$\parallel$	$\perp$	0.110	0.049	0.231	0.080	No
rMK205-1	$\parallel$	-	0.130	0.105	0.260	0.191	Yes
rMK205-2	$\parallel$	-	0.133	0.111	0.263	0.188	Yes, r^{area} outside
rMK205-3	$\parallel$	-	0.132	0.110	0.238	0.172	Yes
rMK205-4	$\parallel$	-	0.150	0.123	0.257	0.164	No

Figures
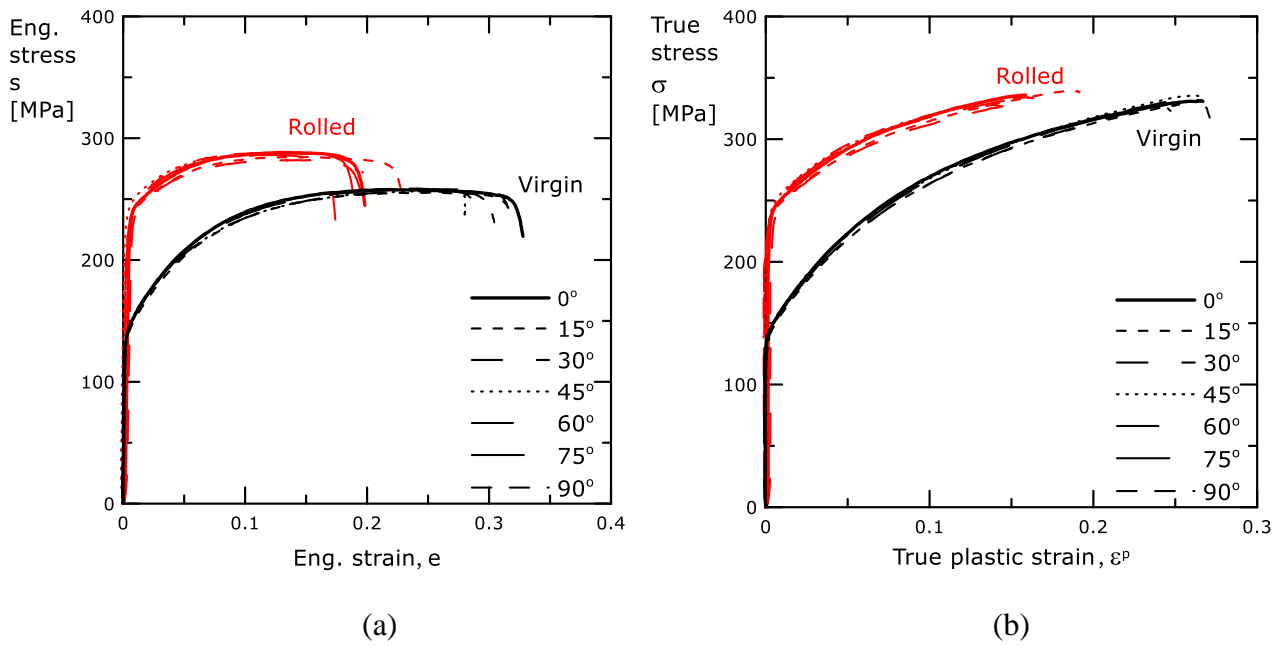
Figure 1   Experimental (a) engineering and (b) true stress-strain curves of virgin and rolled AA6016 for all tested directions.

(a)

(b)
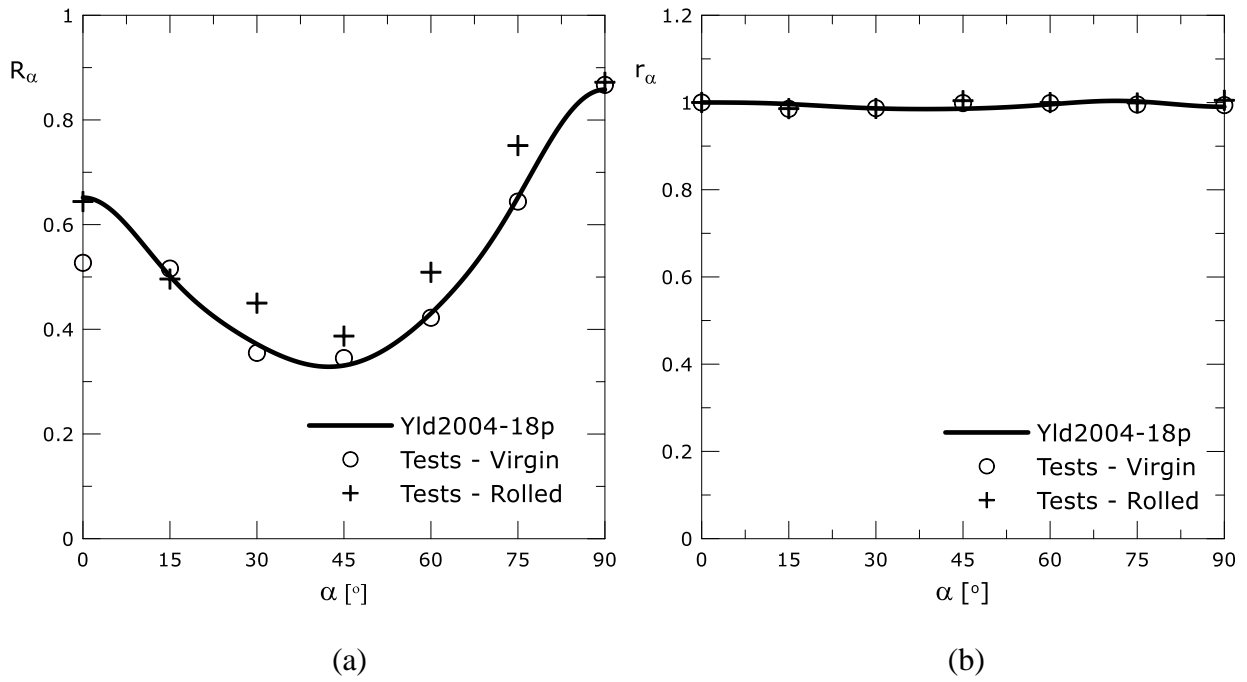
Figure 2   Average experimental and calculated (a) strain ratios R_α and (b) stress ratios r_α, where the calibrated Yld2004-18p function is used in the calculations.
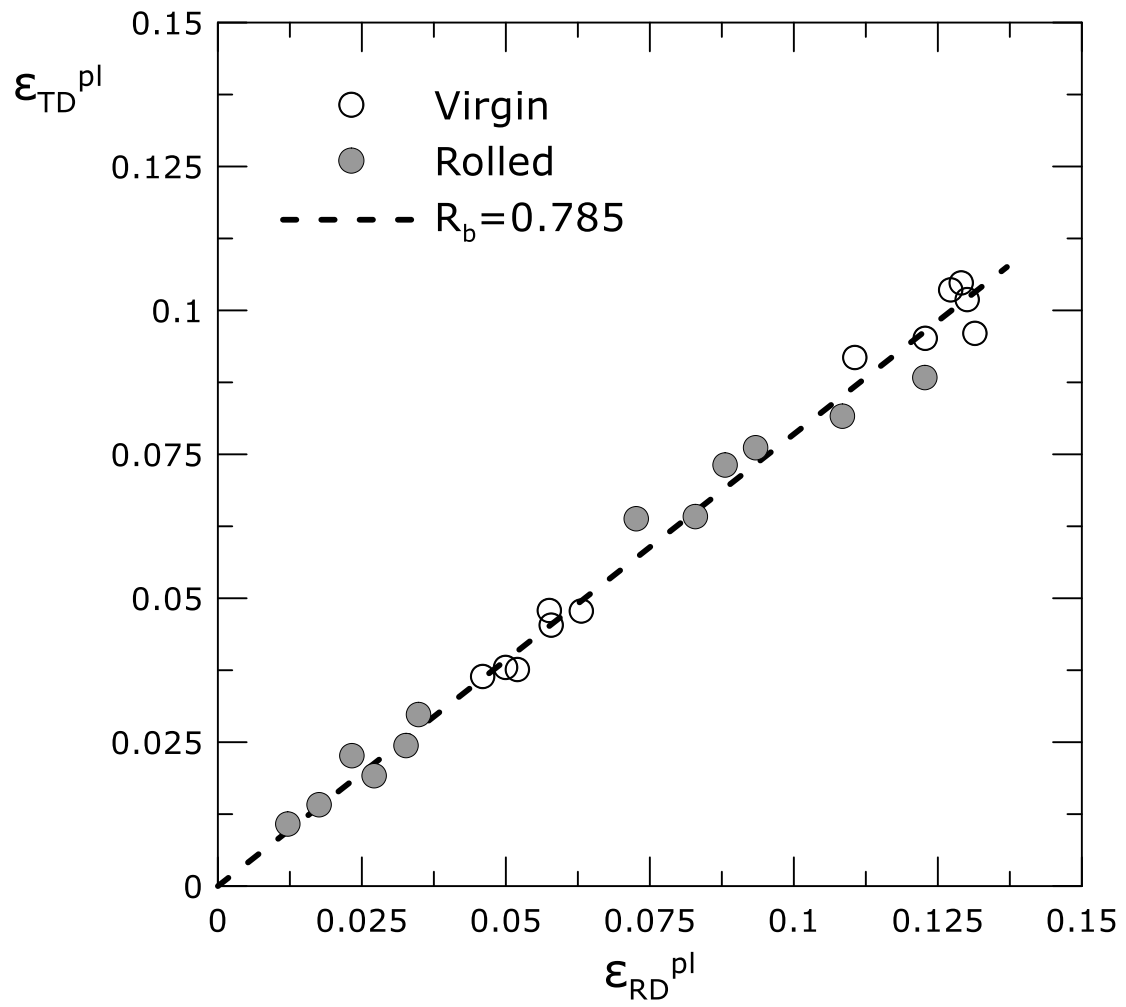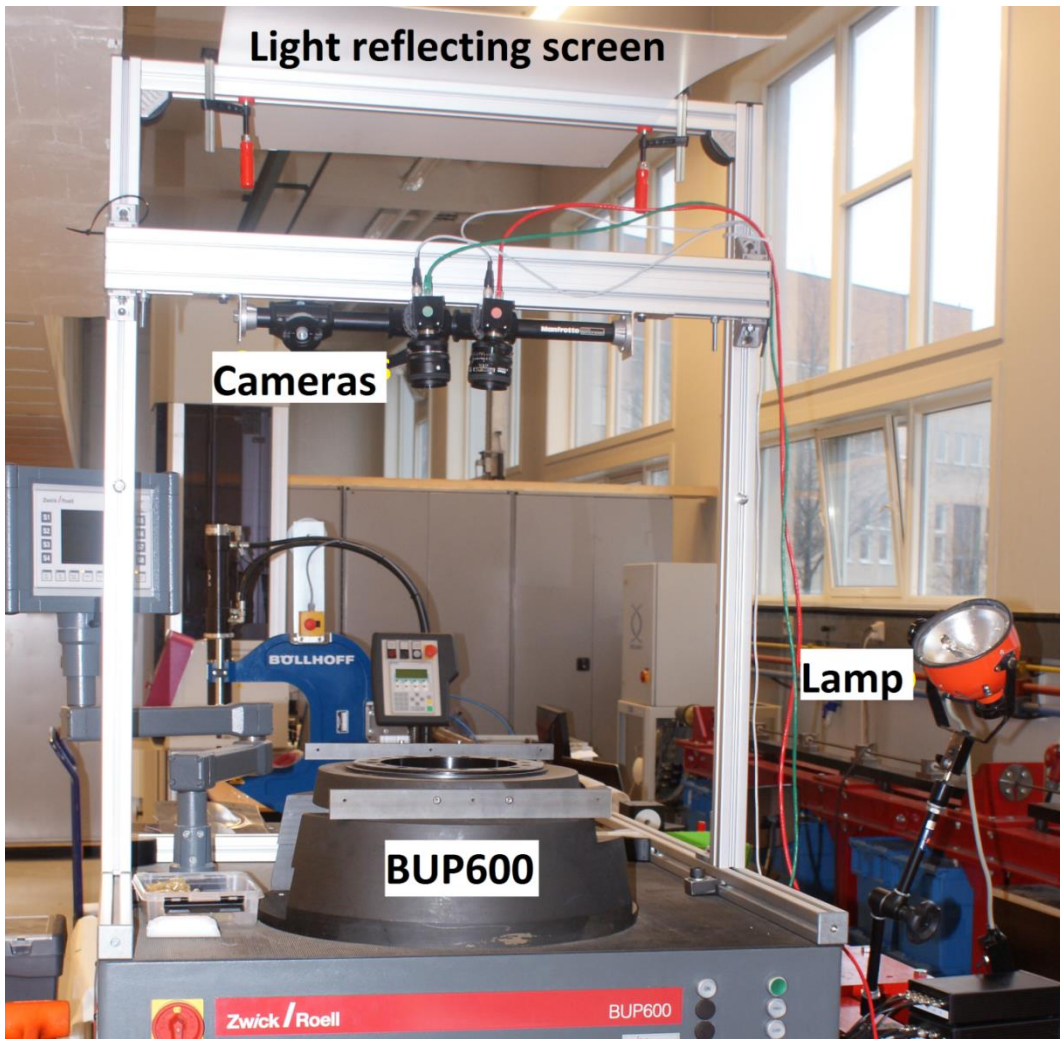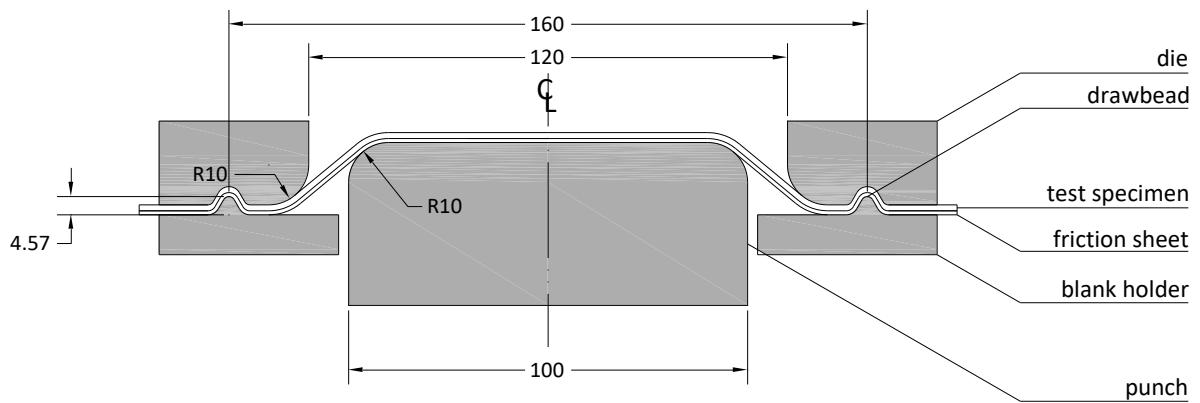
Figure 3   Relation between plastic strains in RD and TD after disk compression tests to different strain levels and linear regression fit to determine R_b.

(a)

(b)

Figure 4   (a) Formability test set-up and (b) Marciniak-Kuczynski test set-up geometry [mm].

Figure 5   Marciniak-Kuczynski samples and underlying friction sheets after testing.
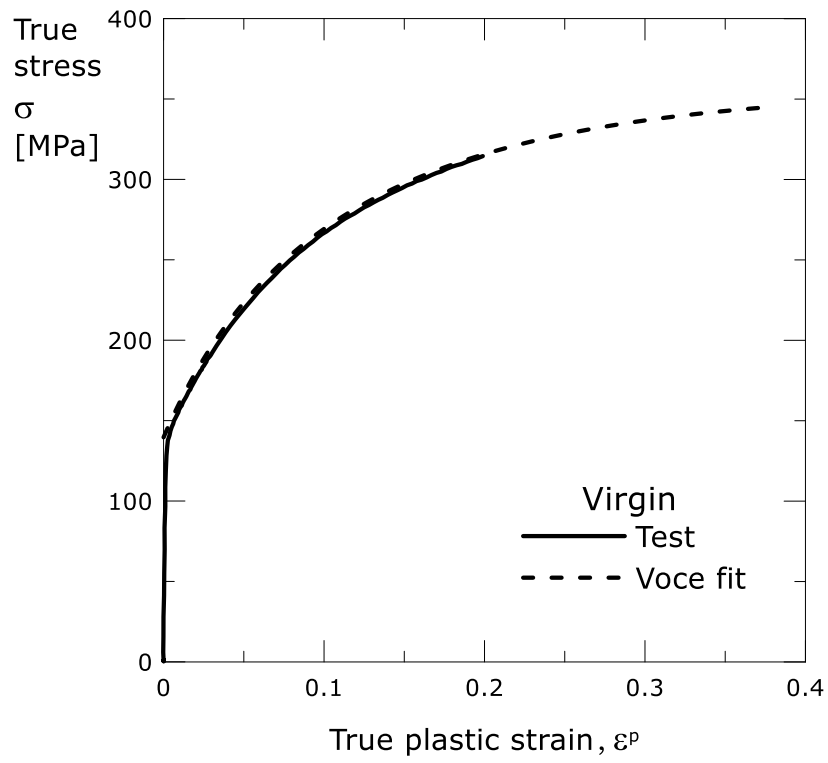
Figure 6   Experimental true stress-strain curve of virgin AA6016 and fitted hardening curve using the two-component Voce rule.
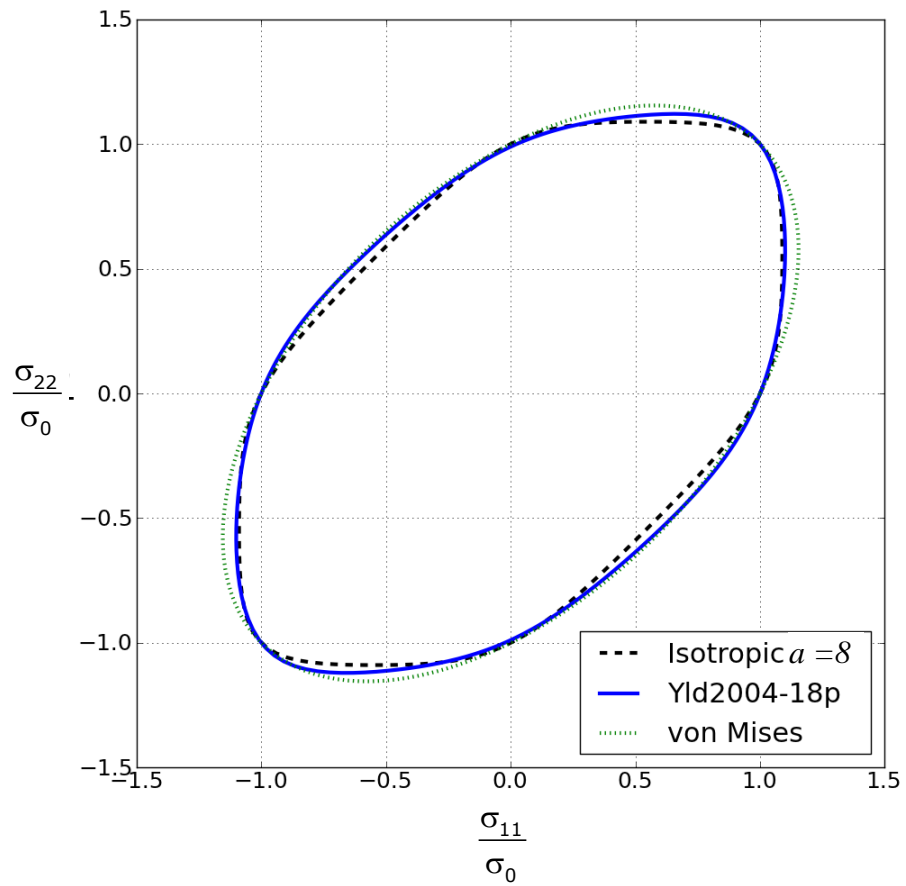
Figure 7   The calibrated Yld2004-18p yield function compared with the isotropic von Mises and
Hershey yield functions. In the figure, the x_1-axis is along RD and the x_2-axis is along TD.

Figure 8   Roping and multiple local necks observed at the bottom side of a Marciniak-Kuczynski sample [19].
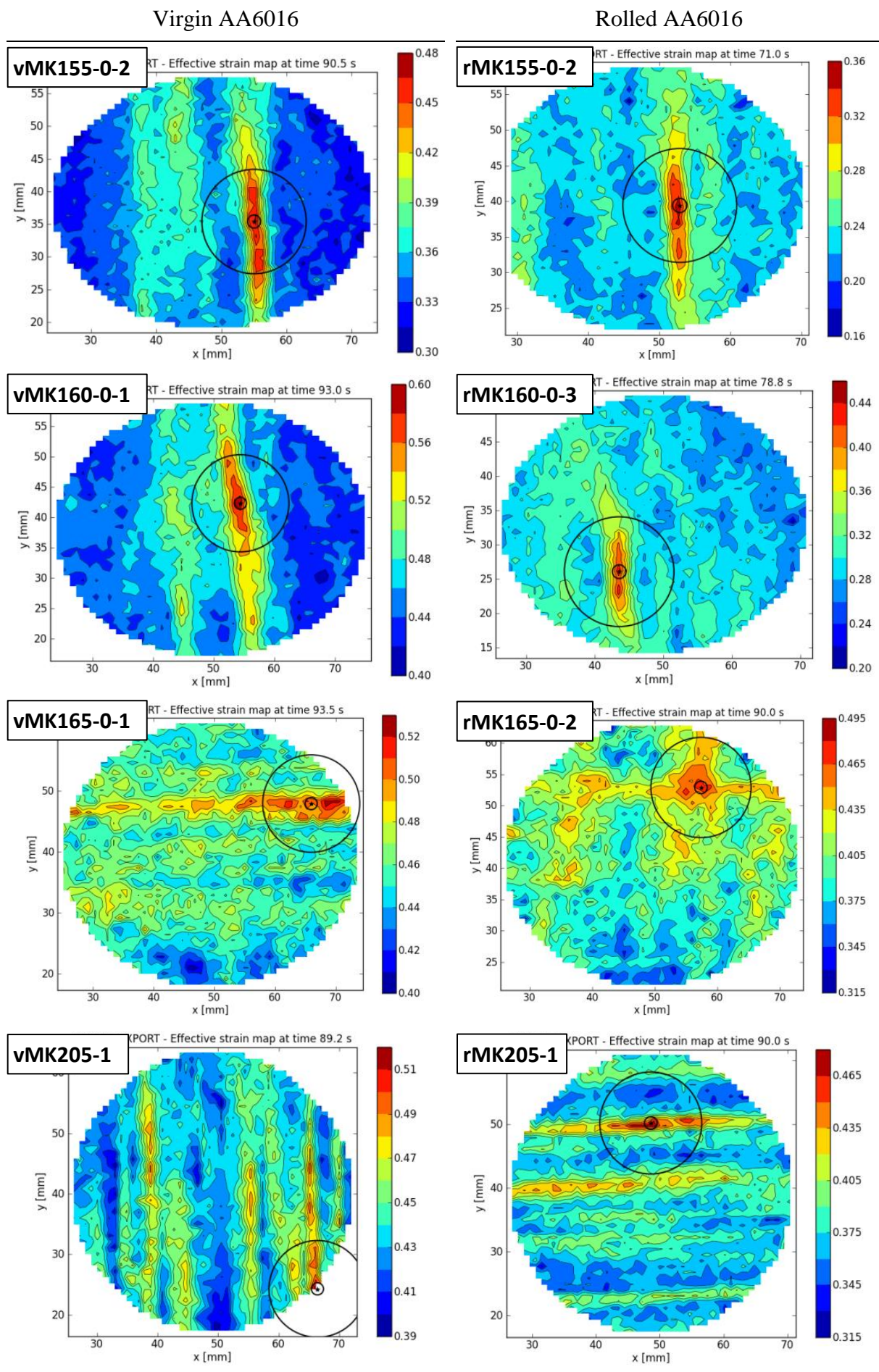
Figure 9   DIC strain maps from the MK tests (parallel to RD) of the virgin and rolled AA6016. Here, the *x*-axis equals RD and the *y*-axis equals TD, except for the strain map for vMK205-1 where the *x*-axis equals TD and the *y*-axis equals RD.

Virgin

Parallel to RD			Normal to RD
vMK160-0-1	vMK165-0-1	vMK165-0-2	vMK165-90-2
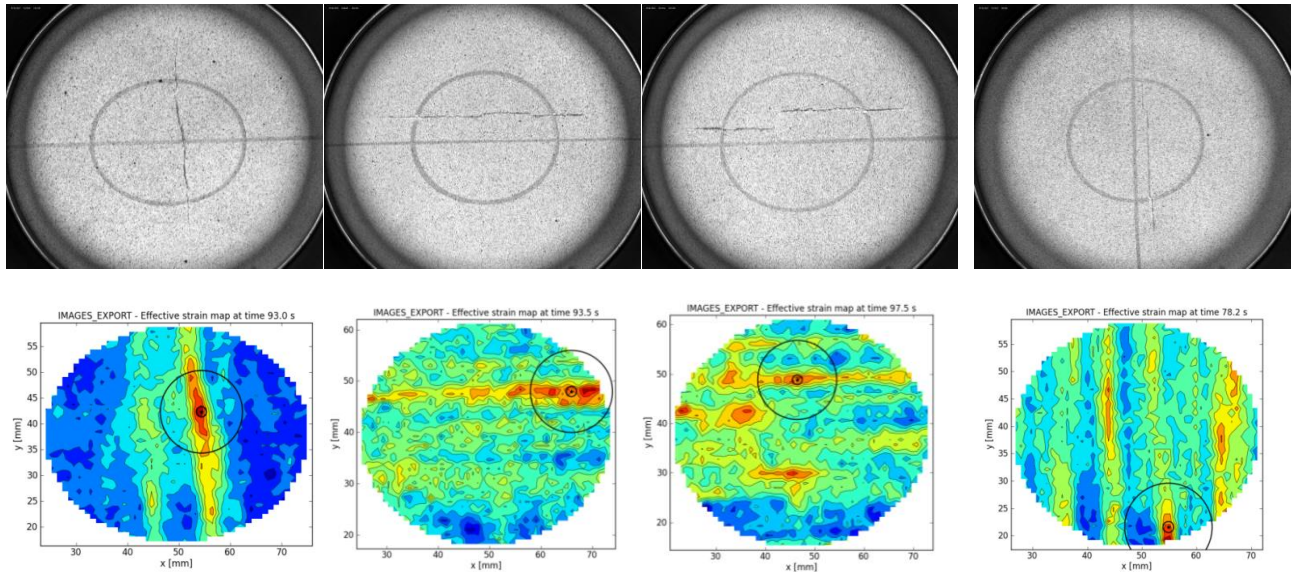
Rolled

Parallel to RD			Normal to RD
rMK160-0-2	rMK165-0-1	rMK165-0-2	rMK165-90-2
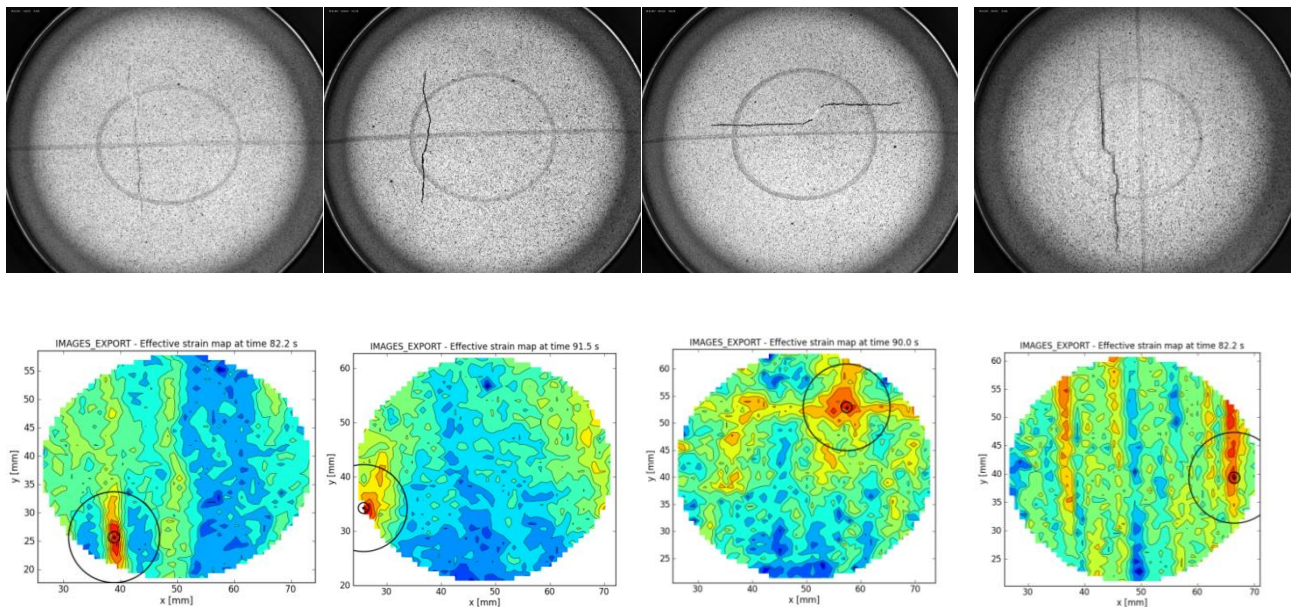
Figure 10 Fracture images and DIC strain maps for some of the MK tests of virgin and rolled AA6016. Here, the *x*-axis equals RD and the *y*-axis equals TD when the major principal strain axis is parallel to RD, while the *y*-axis equals RD and the *x*-axis equals TD when the major principal strain axis is normal to RD.
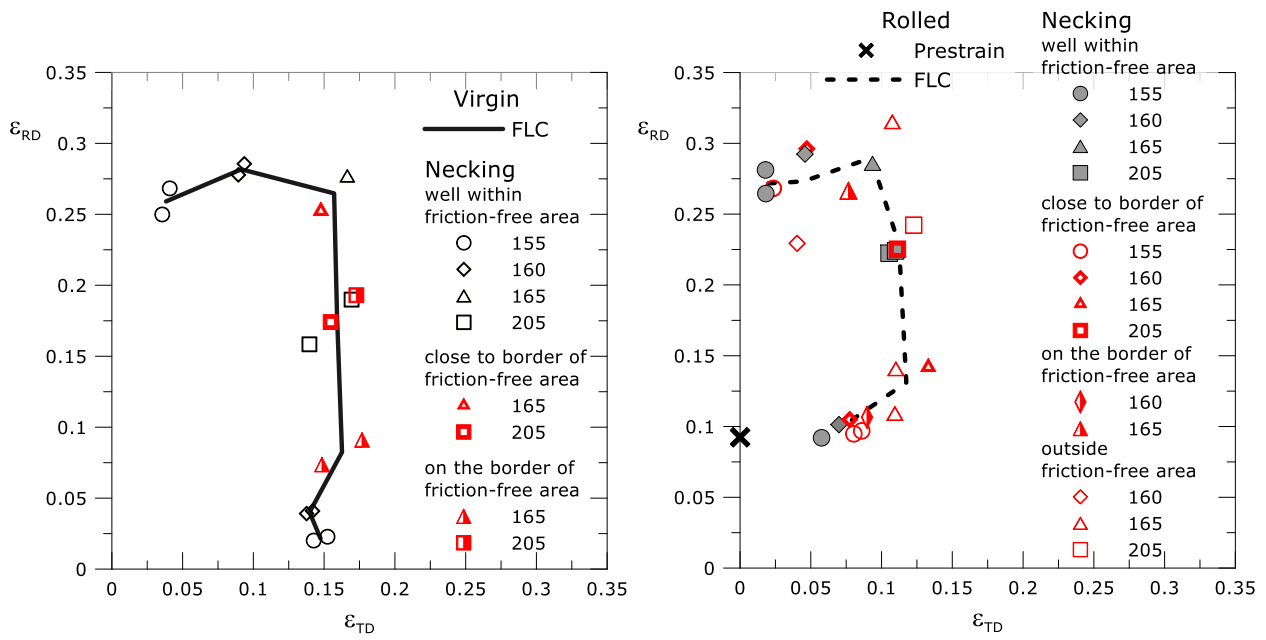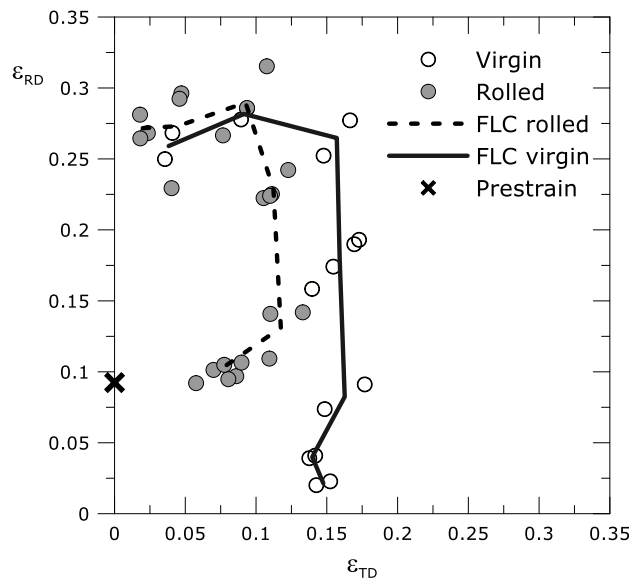
Figure 11 Experimental forming limits strains for (a) virgin and (b) rolled AA6016. (c) Comparison of the FLD for virgin and rolled material.
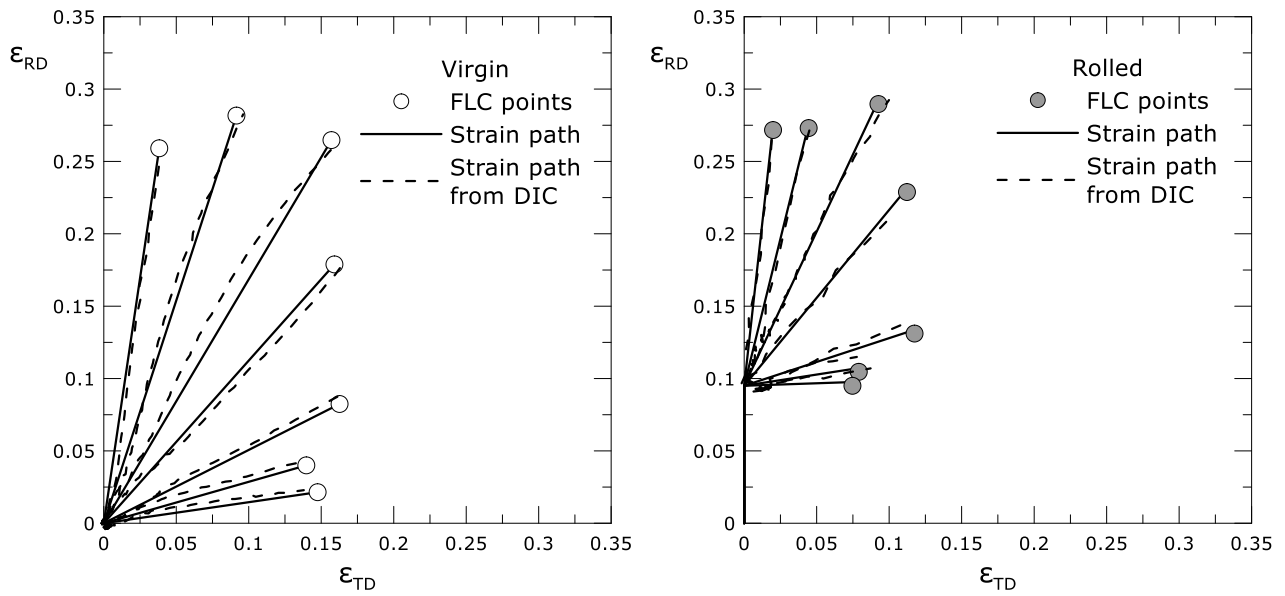
Figure 12   Specified average strain paths used for the mapping into the stress space, and the strain paths for a representative test found from DIC.
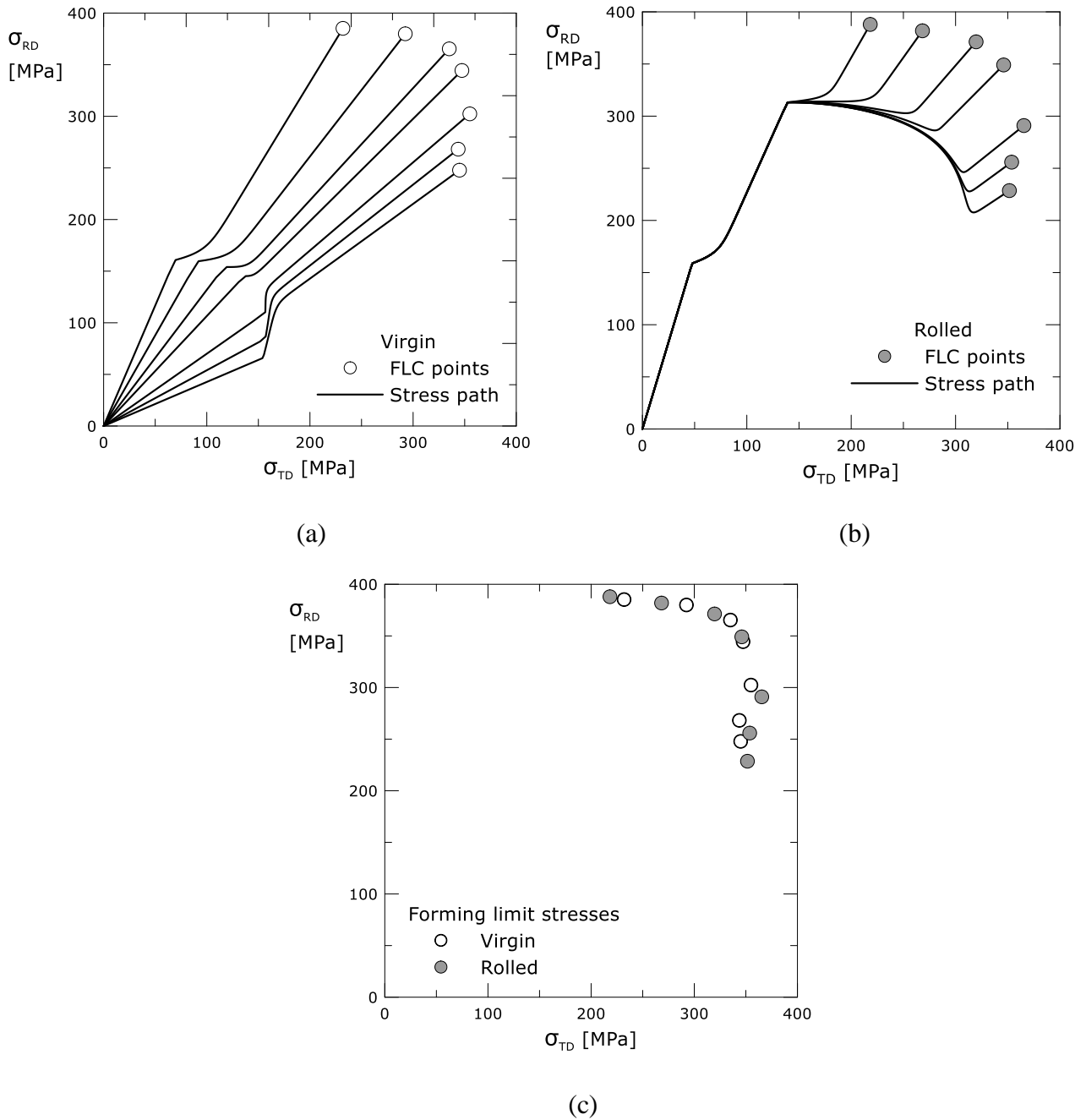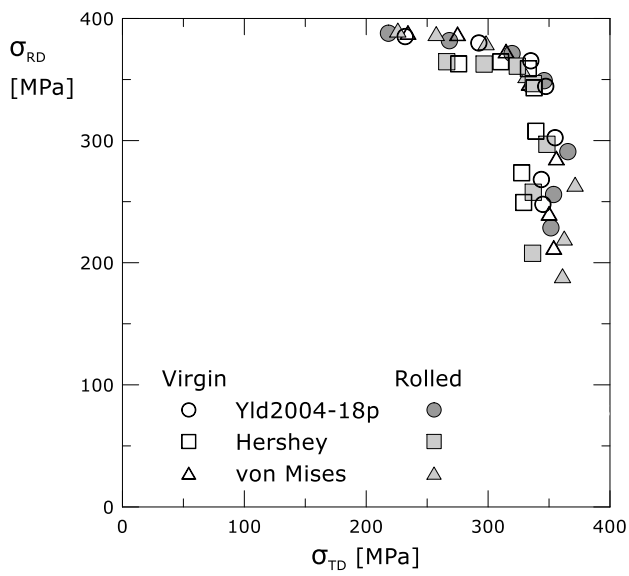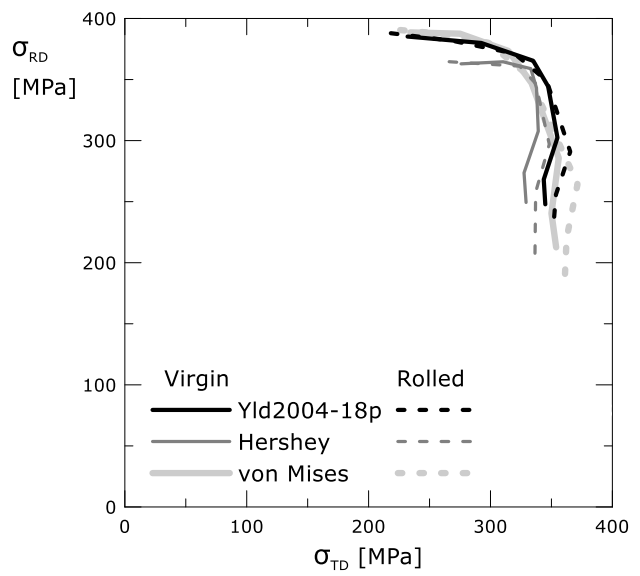
Figure 13   Calculated stress paths for the tests on (a) virgin material and (b) rolled material. (c) The experimentally obtained forming limit stresses of virgin and prestrained AA6016 using the Yld2004-18p criterion.

(a)   (b)

Figure 14   Comparison of experimentally obtained forming limit stresses of virgin and prestrained
AA6016 using different yield criteria to map the limit strains into stress space.
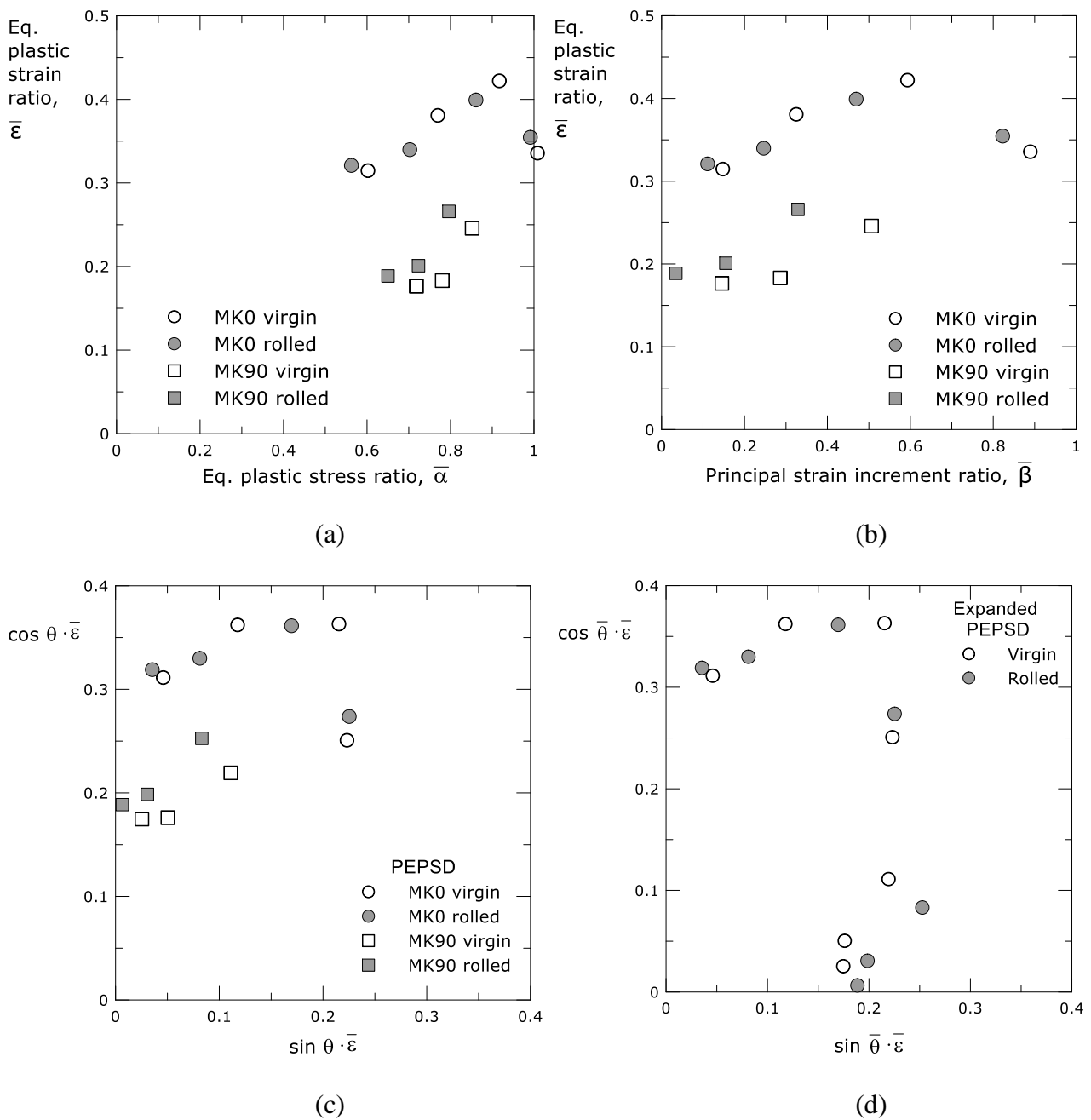
Figure 15 Experimentally obtained forming limits of AA6016 plotted in different EPS-based diagrams: (a) equivalent plastic strain vs. stress ratio, (b) equivalent plastic strain vs. the ratio of principal strain increments, (c) original PEPSD, and (d) expanded PEPSD for anisotropic materials.